Journal of Geophysical Research: Solid Earth

Supporting Information for

Heterogeneity versus Anisotropy and the State of Stress in Stable Cratons: Observations from a Deep Borehole of Opportunity in Northeastern Alberta, Canada

Wenjing Wang[1*], Douglas R. Schmitt[1,3], Judith Chan[2,3]

[1] Earth, Atmospheric, and Planetary Sciences Department, Purdue University, West Lafayette, Indiana, USA, 47907

[2] Earth Signal Processing Ltd., Calgary, Alberta, Canada, T2P 2X6

[3] Formerly, Department of Physics, University of Alberta, Edmonton, Alberta, Canada, T6G 2E1

* Corresponding author: Wenjing Wang (wang4084@purdue.edu)

Contents of this file

Introduction

This supporting information provides details on materials introduced in the main text.

Text S1. Data Sources for Figure 1

A variety of data sources were used to construct Figure 1.

1.1 World Stress Map Data: These were obtained from a limited search at http://www.world-stress-map.org/casmo/ over latitudes from 58°N to 61°N and longitudes from -95°E to -121°E with the data saved as the text option on November 21, 2021. Stress directions provided by breakouts (BO) or drilling induced tensile fractures (DITF) were included in the map.

1.2 Saleski Pilot Project: An average of the directions of DITFs observed in an ensemble of vertical boreholes drilled into the Devonian Grosmont Formation for hydrocarbon production at depths between 300m and 400m were reported by Morin (2017). The center of the ~15 km X 15 km industrial site, referred to as the Saleski Pilot Project, is at 56.370403°N, -112.942834°W and it lies 91 km WSW of the Hunt Well at 56.75955°N, -111.55472°W.

1.3 Aquistore CO_2 Sequestration Project: Interpretations of the Aquistore Observation Well image logs at 49.023°N, -103.085°W were described in Stork et al. (2018).

1.4 Earthquake Epicenters: Epicentral locations were downloaded from the USGS *(https://earthquake.usgs.gov/earthquakes/search/)* for all events of magnitude > 2.5 M_b with delimited geographical locations over latitudes from 58°N to 61°N and longitudes from -95°E to -121°E, and with dates from 1/1/1980 to 11/20/2021. The data downloaded as text option were selected on November 21, 2021.

1.5 Relative Plate Motions: The relative plate motion was found for the location 55°N, -110°W using the online calculator https://www.unavco.org/software/geodetic-utilities/plate-motion-calculator/plate-motion-calculator.html under the GSRM v2.1 model on 11/20/2021.

Text S2. Descriptions of Logging Instruments and Interpretation Criteria

As many readers are not familiar with the tools and methods of geophysical loggings, and this information can be difficult to find, we provide here a brief overview of the different instruments employed and the procedures used in their interpretations.

2.1 Stress around the Wellbore

S_V can be calculated by integrating the weight of rocks from the surface to the depth of interest, shown in Eq. (S1), where g is the gravitational acceleration constant and ρ(z) is the density at the depth z.

$$S_v = \int_0^z \rho(z) g dz \tag{S1}$$

Analyses of BOs (e.g., Gough & Bell, 1982) or DITFs (e.g., Brudy & Zoback, 1999) from caliper and image logs nominally indicate stress directions. Various models exist to describe the stress concentrations for different levels of complexity starting with Kirsch (1898) solutions for a hole in a thin plate to more elaborated 3D descriptions for arbitrarily aligned boreholes by Hiramatsu and Oka (1962) in isotropic and Amadei (1983) in anisotropic rock masses. Principles of extracting stress information from drilling induced failure patterns typically often rely on the Kirsch equations (1898) that provide analytical solutions for stress distribution around a hole in a linear elastic isotropic infinite 2D plate subjected to far-field stresses. When applied in the drilling of a vertical borehole whose axis is aligned with S_V, the effective stresses immediately at the borehole wall in a cylindrical coordinate system are shown in Eq. (S2-S4):

$$\sigma_{rr} = P_w - P_p \tag{S2}$$

$$\sigma_{\theta\theta} = S_H + S_h - 2(S_H - S_h)cos2\theta - P_w - P_p \tag{S3}$$

$$\sigma_{zz} = S_v - 2\nu(S_H - S_h)cos2\theta - P_p \tag{S4}$$

where σ_{rr}, $\sigma_{\theta\theta}$ and σ_{zz} are the Terzaghi effective radial, hoop (circumferential), and axial stresses governing failure with respect to the borehole; θ is the angle measured from the S_H direction; P_w is the fluid pressure in the borehole (i.e., mud pressure); P_p is the pore pressure in the formation, and υ is Poisson's ratio.

2.2 Caliper Measurements

2.2.1 Fullbore Formation Microimager FMI™ (Schlumberger): This instrument was employed in the 1994 and 2003 surveys. Data from this instrument include both high resolution images based on cm-scale variations in electrical conductivity along the borehole and oriented caliper measurements of the borehole diameter in two directions. Details of the physics of this measurement and the geometry of the tool may be found from Schlumberger brochure SMP-5822 at https://www.slb.com/-/media/files/fe/brochure/fmi-br.ashx (accessed December 11, 2021). The orientation of the tool, referred as P1AZ (Pad 1 Azimuth in Horizontal Plane), is provided by magnetometers by correcting to the true north. At the time of measurements, the caliper values came from the extension radius of the four opened electrode pads. The width of the tool assembly may prevent the determination of the maximum borehole elongation if the pads are larger than the breakout.

2.2.2 ICDP Operational Support Group Dipmeter: This instrument was employed in the 2011 survey from 1000 to 1873 m by the Operational Support Group of the International Continental Scientific Drilling program (ICDP-OSG) from the GeoforshungZentrum (GFZ) Potsdam. It is a standard oriented 4-arm caliper with an electrode-bearing pad (34.5 X 79.5 mm) mounted to each caliper arm. The resolution of the caliper is 1 mm. Borehole enlargements wider than 35 mm can be detected while the maximum reading cannot exceed 250 mm. Mature and wide breakouts will lock a pair of pads inside, stopping the tool rotation that is forced by the torque of the logging cable.

2.2.3 Powered Position Calipers PPC™ (Schlumberger): This tool was employed in conjunction with the ultrasonic imaging and dipole shear sonic runs in the 2013 sessions. This is a 4-arm caliper tool in which the arms actively push against the borehole wall to allow for accurate determinations of the widths of the two borehole axes. The width of the arms on this tool allows for it to extend fully into the breakouts. More information on this instrument may be found at https://www.slb.com/-/media/files/fe/product-sheet/ppc-ps (accessed December 11, 2021).

2.2.4 Breakout Interpretation Criteria: Criteria for determining breakouts from caliper logs are modified from those provided by Kerkela and Stock (1996) as follows:

a) The smaller caliper measurement must be within 95%-105% of the bit size.

b) The difference between two caliper measurements is greater than 10 mm.

c) The Pad 1 azimuth (P1AZ) does not change dramatically, that is, the change should be less than 1° over 1 m and P1AZ must be nearly constant for at least 3 m along the borehole.

The first criterion excludes the possibility of identifying washouts as breakouts. The second and third criteria ensure the breakouts identified are relatively large and long, which prohibit us from mistaking the roughness of the wellbore wall as breakouts. The third criterion ensures the tool is locked in the breakout due to the friction between pads and elongated walls. Further, because the Hunt well is nearly vertical, we did not need to worry about mistaking a key seat as a breakout since the spalling along the low side of the borehole is unlikely.

Along undamaged and in-gage sections of a borehole, the cross section is circular with C1 = C2 = BS: the nominal drill bit diameter. In this situation, the wireline torsion typically forces the tool to rotate as it rises during logging so that P1AZ shows no preferential direction. When present, however, uniformly oriented BO ruts trap one caliper arm pair with P1AZ remaining constant and at the same time, either C1 or C2 remains in gage while the diameter of the other arm exceeds BS (Bell & Gough, 1979), but to find α_H from P1AZ, one must consider which arm pair is most extended.

Breakouts will be identified if caliper logs meet the above criteria. In order to get the breakout azimuth, we rely on the tool direction information provided by P1AZ. Calipers measured by two sets of in line pads, pad 1 - pad 3 and pad 2 - pad 4, are denoted as C1 and C2 respectively. If C2 is larger than C1, because P1AZ refers to the pad 1 azimuth, we need to add 90° to represent the breakout direction (longer caliper direction). Otherwise, P1AZ is the same as the breakout direction, which represents the azimuth of the minimum horizontal stress based on Kirsch (1898) equations.

2.3 Borehole Wall Imaging

2.3.1 Fullbore Formation Micromager FMI™ (Schlumberger): The calipers attached to this instrument were described above. In addition, the image data from this instrument consists of high-resolution images based on cm-scale variations in electrical conductivity along the borehole wall. Essentially, the caliper arms on the tool push 4 pads containing 192 button electrodes against the wall rock with the response from these measured continuously as the tool is pulled up along the borehole. Reorganization of these responses forms an image of the local variations in electrical conductivity that may then be interpreted. The image is only provided beneath the zones that the electrodes cover, and in larger diameter boreholes this coverage is incomplete, leaving gaps between strips with no data as shown, for example, in Figure 8. This image is oriented in conjunction with the calipers using onboard magnetometers and accelerometers. Resistivity contrasts in FMI logs enable us to detect structural features, rock textures and drilling-induced features.

2.3.2 Ultrasonic Borehole Imager UBI™ (Schlumberger): This instrument was employed in 2013. Ultrasonic imaging tools use a rotating ultrasonic transducer that transmits and receives ultrasonic pulses outward to and reflected from the borehole wall rock. The transducer typically sends a pulse every 2° in azimuth as it rotates, collecting at each point the waveform amplitude and transit time; as such it provides a nearly continuous measure of these attributes around the borehole circumference. The waveform amplitude depends on the relative elastic impedance between the rock and the borehole fluid. Alternatively, the ultrasonic pulse may be scattered by rugose sections on the borehole wall and will be weakened or even not be recorded. The transit time can be easily converted to the borehole radius if the fluid sound speed is known. Two image logs, organized according to depth and azimuth, are further oriented from magnetometer and accelerometer sensors. These oriented images with travel time and amplitude contrasts may be used to measure the azimuths of breakouts or drilling induced tensile fractures and the orientations of planar features such as fractures, sedimentary beds, and foliation planes. Specifically, breakouts result in the elongation of the wellbore and therefore, the emitted ultrasonic pulse must travel a longer distance or it may not return to be recorded as the reflected beam may not intersect the borehole wall surface, normally causing increased travel time and decreased or even vanished amplitude. Further technical information on the tool used may be found at https://www.slb.com/-/media/files/fe/brochure/ubi-br.ashx (accessed December 11, 2021) or https://brgvm17.ldeo.columbia.edu/research/technology/schlumberger-wireline-tools/ultrasonic-borehole-imager-ubi/ (accessed December 11, 2021).

Image processing of image logs was performed using the WellCAD™ 5.3 (Advanced Logic Technology, Luxembourg). The preprocessing steps are as follows:

a. Orient image logs to true north using Pad 1 Azimuth in Plane Orthogonal to Tool Axis (P1NO).

b. Apply a despiking filter to image logs with 80% cutoff high and 20% cutoff low in a 3 X 3 points filter window.

c. Dynamic normalization with a 20 cm-height sliding window to enhance the local contrast using a histogram normalization.

Two types of low-quality images were excluded before interpreting drilling induced failures. The first type of low-quality images is caused by the local magnetic field variation. Image logs depend largely on the magnetometers and accelerometers/inclinometers to orient to the true geographic direction. If the magnetic field varies, the correction from P1NO to the true north direction will be erroneous. Therefore, whenever there is a magnetic field inclination or intensity anomaly, the corresponding depth was left out to improve the image quality. The other type of low-quality images is due to the signal loss represented by white patches existing in image logs. The signal loss is mostly caused by a wide wellbore diameter due to large breakouts or major faults (Azzola et al., 2019). The sonic beam energy will be strongly scattered when a wellbore diameter is rather large, and it is difficult to see the reflected echoes in UBI logs.

After excluding the above-mentioned low-quality images, ultrasonic image logs were examined every 20 cm vertically without overlapping to find drilling induced failures. Breakouts are represented by a pair of 180°-separated wide zones with smaller amplitudes and longer travel times of the reflected echo compared to the original wellbore radius whereas drilling induced tensile fractures (DITFs) are narrow. The azimuth of drilling induced failures at each 20 cm-depth interval was selected to be the median and was discarded if drilling induced failures were shorter than 20 cm. Breakout width and azimuth are illustrated in Figure 4. In the image interpretation, the breakout width was marked by the furthest extent of failure zones and the breakout azimuth was represented by the azimuth of the middle point of failure zones. The width determination of DITFs is not necessary since it is narrow.

2.3.3 Dipole Shear Sonic Imager DSI^{TM} (Schlumberger): This tool was run in 2013. It contains one omnidirectional monopole transmitter and two pairs of orthogonally oriented unidirectional dipole transmitters. The pulsed waveforms from these are received by an array of hydrophones, which provides an ensemble of waveforms that are variously processed, yielding the monopole P- or S-wave speeds or the crossed-dipole fast and slow S-wave speeds. Additional details on the operation of this tool may be found at https://brgvm17.ldeo.columbia.edu/research/technology/schlumberger-wireline-tools/dipole-sonic-imager-tool-dsi-2/ (accessed December 11, 2021) or at https://www.slb.com/-/media/files/fe/product-sheet/dsi-ps.ashx (accessed December 11, 2021).

Dispersion curves provide the evidence of formation anisotropy. Slowness of the fast and slow dipole flexural waves overlaps if the formation is isotropic, or the wellbore is aligned with the symmetric axis of the transverse isotropic formation (Figure S1a). In these two cases, there is no shear wave speed difference for all propagation directions. However, slowness of the fast and slow dipole flexural waves separates and runs roughly parallel to each other if the formation is intrinsically anisotropic and the wellbore axis is at an angle to the formation symmetric axis. In this scenario, the polarized shear wave travels faster along the direction parallel to the mineral alignment compared with the direction perpendicular to that (Figure S1b). Lastly, if the anisotropy is stress induced due to the nonlinear response between stress and strain for the rock, then the slowness of the fast and slow dipole flexural waves has a crossover (Sinha et al., 1994; Winkler, 1997), shown in Figure S1c. Lower flexural wave frequencies are more sensitive to the originally far-field stresses while high frequencies are more sensitive to the near-borehole stresses, which are a reverse of the originally far-field stresses due to the stress concentration around the wellbore. Fang et al. (2015), however, discussed some issues with the interpretation of the crossover curve based on the numerical modelling that includes borehole geometry.

Boness and Zoback (2004, 2006) compared shear wave anisotropy and polarizations to the orientations of bedding planes and fractures from high resolution electrical conductivity image logs through fractured granites and tilted sediments in the SAFOD project, concluding that the anisotropy both local and, based on other seismic measurements, more distant from the borehole was controlled by the state of stress. In drilling of the igneous oceanic crust near midocean ridges in the Atlantic and Indian oceans, Iturrino et al. (2005) interpreted variations in the fast shear wave azimuth χ_F to be controlled by either rock mass texture or the directions of regional compression depending on the depth. H.-Y. Wu et al. (2007) and Y.-H. Wu et al. (2008) linked changes in anisotropy and χ_F to the severity of shale bedding dip and fractures in the vicinity of the inferred Chi-Chi earthquake slip zone; and they linked abrupt rotations in χ_F to variations in lithology and structure. Goswami et al. (2019, 2020) carried out an extensive logging campaign through igneous Deccan traps and into granitic basement near Koyna, India. They found correlations between fractures, stress directions inferred from BOs and DITFs, dipole shear wave anisotropy and χ_F. However, to the best of our knowledge, there are scant comparable studies in the literature in which these differing logging methods have been used in a combined analysis in cratonic metamorphic terranes.

2.4 Geophysical Logs

2.4.1 Natural γ-ray Tool: This tool measures the level of natural radioactivity from the rock mass that originates from naturally occurring unstable isotopes of U, Th, and K. The instrument is almost always employed in logging campaigns since the repeatable response is often used as the depth standard, against which various different logging runs may be calibrated. The calibrated instrument reports the level of radioactivity on a relative scale of American Petroleum Institute (API) units.

2.4.2 Photoelectric Factor Tool: The photoelectric factor P_e is a semi-quantitative measure of the elemental composition of the material surrounding the borehole, and is based on the attenuation of soft γ-rays, the absorption of which within the electronic shells of the elements is accommodated by the expulsion of a "photo-electron". Essentially, the P_e depends on the atomic number Z according to $P_e = [Z/10]^{3.6}$ and hence the value is highly sensitive to the elements in the minerals of the rock. One advantage of this measure is that the influence of density is mostly removed and therefore the observation can provide some insights into the composition. Discussions of this tool primarily focus on interpretations in sedimentary environments where the principal minerals may be quartz, calcite, or dolomite. Applications to crystalline environments are not so common, but a listing of P_e values for other minerals appears at http://www-odp.tamu.edu/publications/209_IR/chap_02/chap_02.htm (Accessed December 11, 2021).

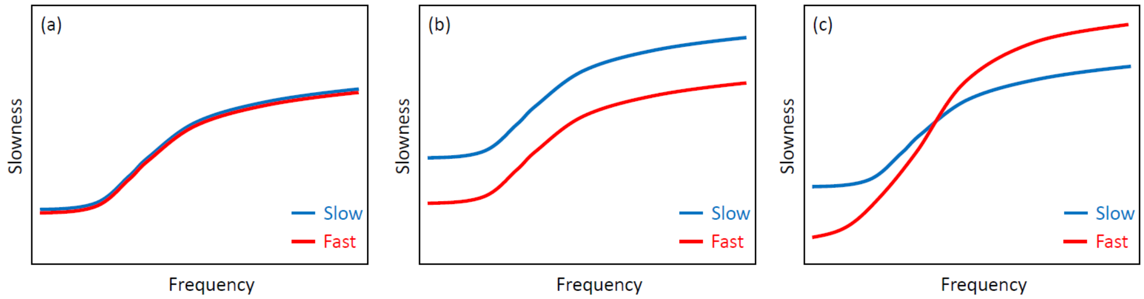

Figure S1. Representative dispersion plots displaying fast (red) and slow (blue) flexural wave slowness as a function of frequency. (a) overlapping pattern in the isotropic case or in the case where the wellbore is aligned with the axial symmetry axis of a transversely isotropic formation (b) separated and parallel pattern in the intrinsic anisotropic case (c) crossover pattern in the stress-induced anisotropic case.

Table S1. Standard Isotropic Equations for Calculating Elastic Moduli

Elastic moduli	Equations
Shear modulus μ (SMG)	$\mu = \rho V_S^2$
Bulk modulus K	$K = \rho\left[V_P^2 - \frac{4}{3}V_S^2\right]$
Young's modulus E (YME)	$E = \frac{9K\mu}{3K + \mu} = 3\rho\frac{\left[V_P^2 - \frac{4}{3}V_S^2\right]V_S^2}{V_P^2 - V_S^2}$
Poisson's ratio ν (PR)	$\nu = \frac{E}{2\mu} - 1 = \frac{1}{2}\frac{V_P^2 - 2V_S^2}{V_P^2 - V_S^2}$

Table S2. Completion History of the Hunt Well – Expanded from Chan (2013)

Event	**Date**	**Remarks**
Drilling Session #1		UWI: 00/07-32-089-10W4/0 Company: Archean Corporation KB: 409.3 m TVD: 1649.0 m Mud Density 1060 kg/m^3 to 1100 kg/m^3
Spud date	Sept. 1, 1994	
Rig on site	Early Sept., 1994	
Drilling began	Early Sept., 1994	
Casing #1	Sept. 1, 1994	Casing liner outside diameter 339.7 mm Shoe set depth: 94 m
Casing #2	Sept. 10, 1994	Casing liner outside diameter: 244.5 mm Shoe set depth: 598.2 m
Drilling completed	Oct. 8, 1994	At 1649.0 m
Service rig released	Oct. 8, 1994	

Rig on site	Oct. 8, 1994	For Schlumberger logging
Logging (Schlumberger)	Oct. 8, 1994	Run #1: DLL, MSFL Run #2: CNL, LDT, NGT Run #3: FMI
Drilling operations suspended temporarily	Oct. 9, 1994	
Rig released	Oct. 10, 1994	
Suspended drilling operations	Nov. 2, 1994	Suspended indefinitely. Bridge plug set at 540 m

Archean Corporation renamed to Anhydride Corporation on June 10, 1996.
Director: Mr. C. Warren Hunt

Drill out permanent bridge plugs and test intervals in granite formation

Rig on site	Sept. 25, 2002	
Drill out cement	Sept. 27, 2002	From 533.55 to 539.59 m
Drill out bridge plug 1	Sept. 27, 2002	At 539.59 m
Drill out bridge plug 2	Sept. 28, 2002	At 596.23 m
Clear tight spots	Sept. 29 – 30, 2002	From 1187.48 to 1216.16 m, and possibly a few other tight spots between 1283.29 to 1640 m
RIH with inflate straddle packer	Oct. 2, 2002	
Swab tests	Oct. 2 – 8, 2002	
Packer test	Oct. 7, 2002	Bottom of top packer at 873.0 m, pressurized at different feed rates. ISIP reported at 7 MPa dropping to 5.5 MPa in 13 minutes
Packer test	Oct. 11, 2002	Bottom of top packer at 1370 m, pressurized at 11.5 MPa, held pressure for long time without dropping
Rig released	Oct. 15, 2002	
Drilling Session #2		UWI: 00/07-32-089-10W4/2 KB: 409.3 m TVD: 2363.3 m Mud Density 1005 kg/m^3 to 1040 kg/m^3
Spud date	Dec. 13, 2002	
Drill out cement and bridge plug	Dec. 16, 2002	

Drilling began	Dec. 17, 2002	Bit size: 222 mm, TVD: 1649 to 1654 m Bit size: 200 mm, TVD: 1656.4 to 2347 m Bit size: 199 mm for coring
Coring #1	Dec. 20, 2002	Recovered 1.22 m core between 1656.4 to 1657.82 m
Coring #2	Jan. 5-6, 2003	Recovered 2.17 m core between 2347.52 to 2350.21 m
Coring #3	Jan. 7, 2003	At 2351 m
Logging (Schlumberger)	Jan. 7, 2003	Run #1: FMI and DSI logs from 2351 to 1600 m Run #2: TLD, CNL, NGT, HRLA, CAL logs from 2351 to 1600 m
Coring #4	Jan. 8-9, 2003	Recovered 11.92 m core from 2351.42 to 2363.34 m
Drilling completed	Jan. 9, 2003	At 2363.3 m
DST #1	Jan. 9-10, 2003	From 1755 to 1800 m
DST #2	Jan. 10-11, 2003	From 2345 to 2363 m
DST #3	Jan. 11-12, 2003	From 1640 to 1664 m, miss run
DST #4	Jan. 12, 2003	From 1645 to 1670 m, miss run
DST #5	Jan. 13, 2003	From 1640 m to 1683 m, bottom hole sample showed ground-up granite and small speckles of metal of unknown source
DST #6	Jan. 13-14, 2003	At 2363 m
Set bridge plug	Jan. 15, 2003	At 590 m
Rig released	Jan. 15, 2003	
Completion and Workover **Drill out permanent bridge plug at 590 m KB, swab and evaluate open hole**		
Rig on site	Jan. 30, 2003	
Production tubing running in hole (RIH)	Feb. 8, 2003	Tubing size: 89 mm Tubing collar: 0.15 m Tubing bottom: 2329.06 m
Hole camera	Feb. 24-25, 2003	Fluid entry found at 632.09 to 640.0 m, 647.94 to 754.81 m, 769.64 to 788.56 m. Possible inflow at 1646 m, 1550 m. No inflow at intervals tested below 1645 m.
Casing #3	Feb. 28, 2003	Casing liner outside diameter: 177.8 mm Shoe set depth: 1005.7 m
Run in production tubing	Mar. 5, 2003	
Rig released	Mar. 14, 2003	

Swab rig in	Mar. 17, 2003	Continued swabbing but little additional fluids produced
Swab tests	Feb. 9 – Mar. 20, 2003	Extensive swabbing, could not recover any additional fluids on last runs, total fluid swabbed is 66.71 m^3 of salt water with no signs of oil or gas
Swab rig out	Mar. 20, 2003	
2004 – 2008: Temperature measurements were made by GeoPos at unknown date. Data is not available.		

Temperature Logging (See Majorowicz et al., 2014)

Temperature logging #1	Dec. 7-9, 2010	Initial run into borehole did not encounter fluid level until 2192 m as indicated by pressure and temperature curves. Casing collar locator (CCL) confirms that production tubing remains in place. Pumped 51-52 m^3 of water into borehole over two days and logged from surface to 2333.7 m Standard logging package included pressure, gamma ccl, temperature and lightning unit including travel time. LSAT Lonkar spectral log Fluid level dropped rapidly. Measured water level at 928 m on Dec. 12, 2010.
Temperature logging #2	Jun. 14-15, 2011	Repeat temperature log to check on the thermal stability of the well. The well was topped up ~2 weeks with municipal water before logging date. Logging as above Fluid level was observed at ~ 65 m.
Remove Production Tubing and Slim Tool Logging		
Rig on site	Jul. 8, 2011	
Removal of production tubing	Jul. 8-9, 2011	248 production tubes removed prior to open hole logging
Rig released	Jul. 9, 2011	
Logging (ICDP-OSG)	Jul. 13-16, 2011	Logging and Vertical Seismic Profiling Carried out by Operational Support Group, GFZ Attempt ultrasonic borehole image log, but centralization springs unable to open

		sufficiently in large diameter below casing. See Chan (2013) for a list of logs and Chan & Schmitt (2015) for descriptions of VSP measurements. Blockage at 1360 m prevents some logs from being run.
Phase 1 Environmental Site Assessment	October 22, 2012	Done by WorleyParsons
Clear Blockage and Commercial Logging		
Service rig on site	November 5, 2013	
Clear blockage	November 7, 2013	Flush well to prepare for logging
Logging	November 8, 2013	Open hole logging from 1005 to 2315 m. New data presented in this manuscript.
Rig released	November 9, 2013	

Note. This material is extracted from the summary of Appendix A of Chan (2013) but updated to include the additional geophysical logging activities described earlier from late November 2013.

Text S3. Calculations for Figure 6

Figure 6 shows how the *P*-, the S_H- and the S_V- wave speeds of vertical propagation change in two examples of foliated metamorphic rocks with the dip angle β_m. We calculated these velocities using both a general program that solves the eigenvalues of the Christoffel equation and the direct analytic solutions for the phase velocities (e.g., Thomsen, 1986):

$$V_{SH}(\beta_m) = \left[\frac{C_{66}\sin^2\beta_m + C_{44}\cos^2\beta_m}{\rho}\right]^{1/2} \tag{S5}$$

$$V_{SV}(\beta_m) = \left[\frac{(C_{11}+C_{44})\,sin^2\,\beta_m + (C_{33}+C_{44})\,cos^2\,\beta_m - D(\beta_m)}{2\rho}\right]^{1/2} \tag{S6}$$

$$V_P(\theta) = \left[\frac{(C_{11}+C_{44})\,sin^2\,\beta_m + (C_{33}+C_{44})\,cos^2\,\beta_m + D(\beta_m)}{2\rho}\right]^{1/2} \tag{S7}$$

$$D(\beta_m) = \sqrt{[(C_{11}-C_{44})\,sin^2\,\beta_m - (C_{33}-C_{44})\,cos^2\,\beta_m]^2 + 4(C_{13}+C_{44})^2\beta_m\,cos^2\,\beta_m} \tag{S8}$$

Note that the Thomsen's parameter δ is also given for the two samples in Figure 6. This is a measure of the wave speed surface curvature at angles away from the principal directions of the material (here parallel and perpendicular to the foliation plane), which is given by:

$$\delta = \frac{(C_{13}+C_{44})^2 - (C_{33}-C_{44})^2}{2C_{33}(C_{33}-C_{44})} \tag{S9}$$

where the C_{ij} is the value of the elastic stiffness (in GPa) of the Voigt reduced notation for a TI medium:

$$C = \begin{bmatrix} C_{11} & C_{11}-2C_{66} & C_{13} & 0 & 0 & 0 \\ C_{11}-2C_{66} & C_{11} & C_{13} & 0 & 0 & 0 \\ C_{13} & C_{13} & C_{33} & 0 & 0 & 0 \\ 0 & 0 & 0 & C_{44} & 0 & 0 \\ 0 & 0 & 0 & 0 & C_{44} & 0 \\ 0 & 0 & 0 & 0 & 0 & C_{66} \end{bmatrix}$$

For the Hunt Well sample with density ρ = 2620 kg/m^3, the values measured at elevated confining pressure by Chan (2013) are:

$$C = \begin{bmatrix} 87.4 & 39.6 & 18.3 & 0 & 0 & 0 \\ 39.6 & 87.4 & 18.3 & 0 & 0 & 0 \\ 18.3 & 18.3 & 68.0 & 0 & 0 & 0 \\ 0 & 0 & 0 & 19.9 & 0 & 0 \\ 0 & 0 & 0 & 0 & 19.9 & 0 \\ 0 & 0 & 0 & 0 & 0 & 23.9 \end{bmatrix}$$

The second sample is from as yet unpublished results on a mylonite sample near the Alpine Fault, New Zealand with density ρ = 2750 kg/m^3 with

$$C = \begin{bmatrix} 98.2 & 24.03 & 10.33 & 0 & 0 & 0 \\ 24.03 & 98.2 & 10.33 & 0 & 0 & 0 \\ 10.33 & 10.33 & 80.61 & 0 & 0 & 0 \\ 0 & 0 & 0 & 30.65 & 0 & 0 \\ 0 & 0 & 0 & 0 & 30.65 & 0 \\ 0 & 0 & 0 & 0 & 0 & 37.09 \end{bmatrix}$$

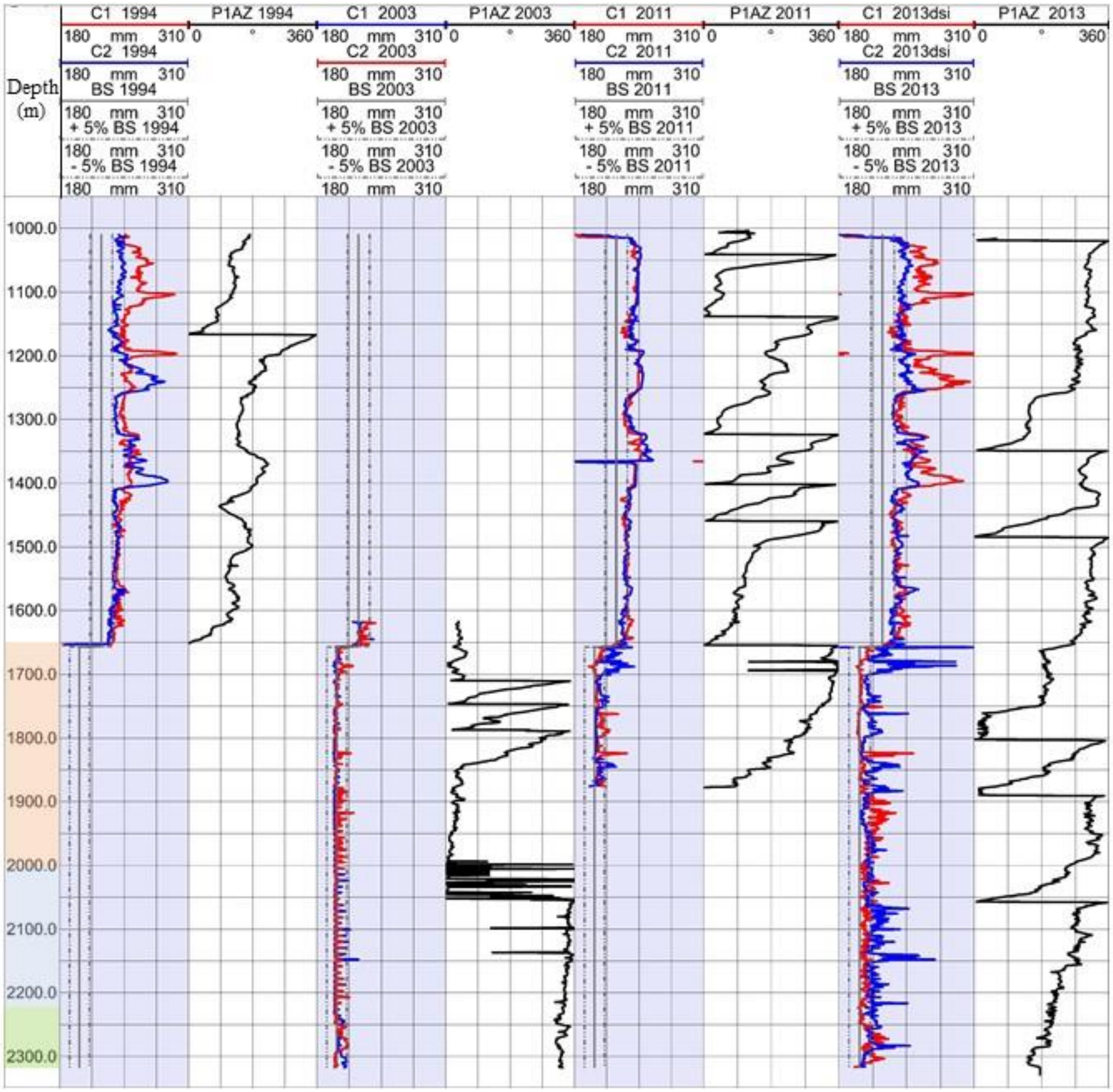

Figure S2. Calipers along with P1AZs from oriented 4-arm caliper logs obtained from the *FMI-1994* and *FMI-2003* runs, the *Dipmeter-2011* run, and the *PPC DSI-2013* run.

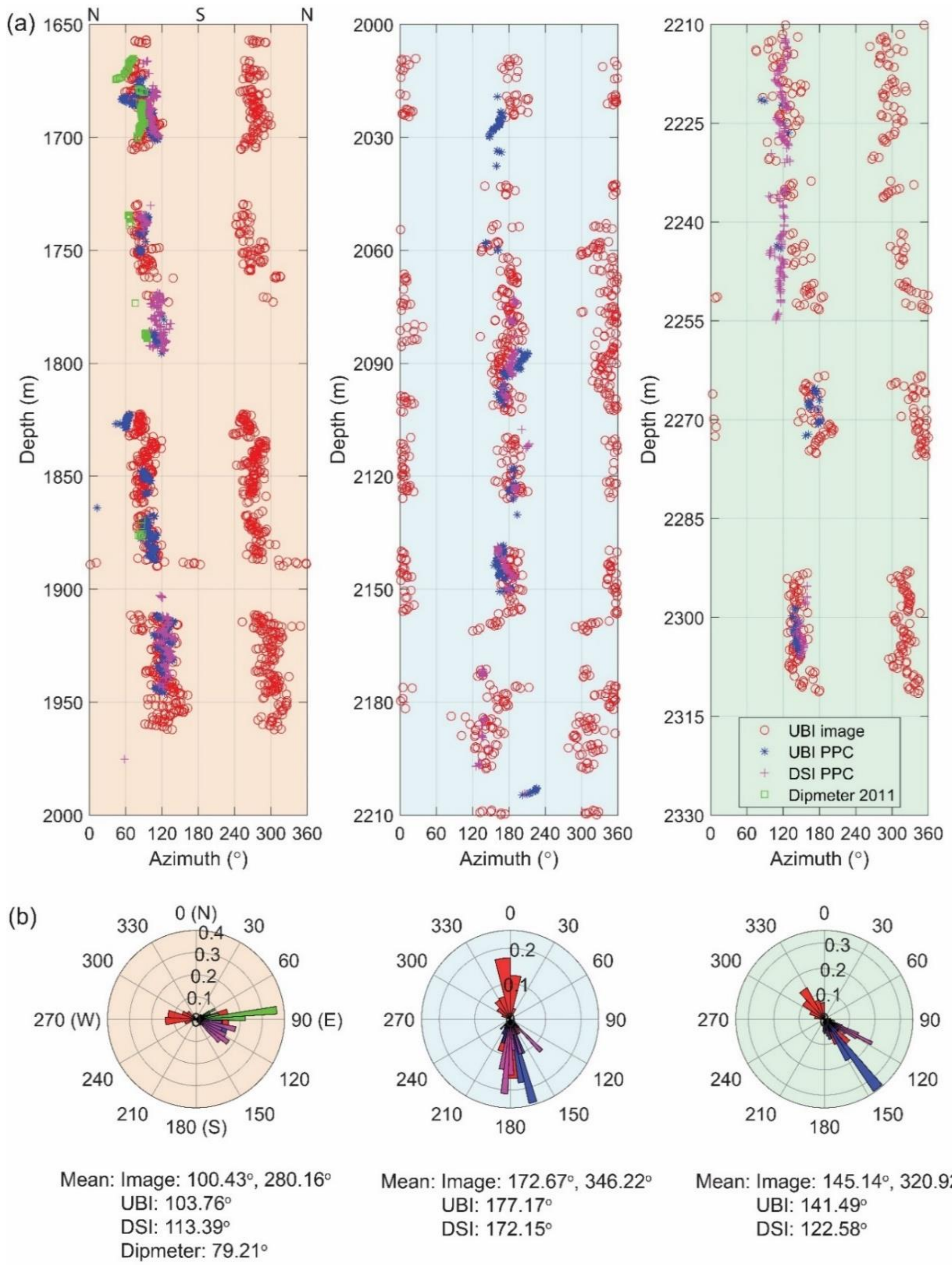

Figure S3. (a) Breakout azimuths from image logs (repeated from Figure 9) and from elongation directions of the consecutive caliper logs. (b) From left to right, the rose histograms represent the BO azimuth distribution at 1650-2000 m, 2000-2210 m, and 2210-2320 m respectively. The color codes follow the color codes in (a).

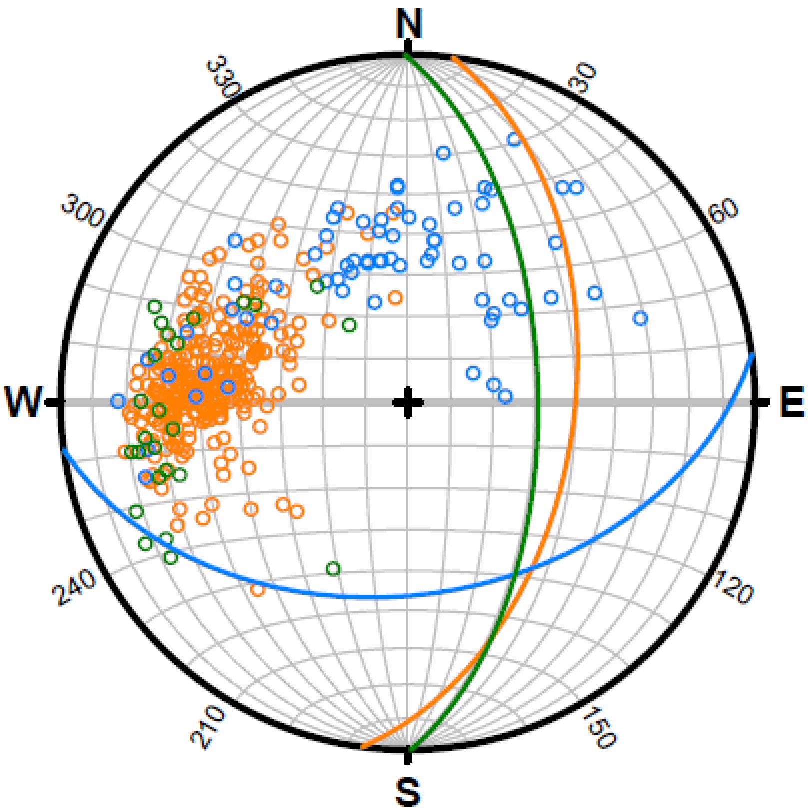

Figure S4. Individual poles used for the calculation of the Kamb contours in Figure 10. Orange, blue, and green hollow circles represent the foliation poles at the depth of 1000-2000 m, 2000-2210 m, and 2210-2330 m respectively. Solid great circles represent the corresponding average foliation orientations at these three depth intervals.

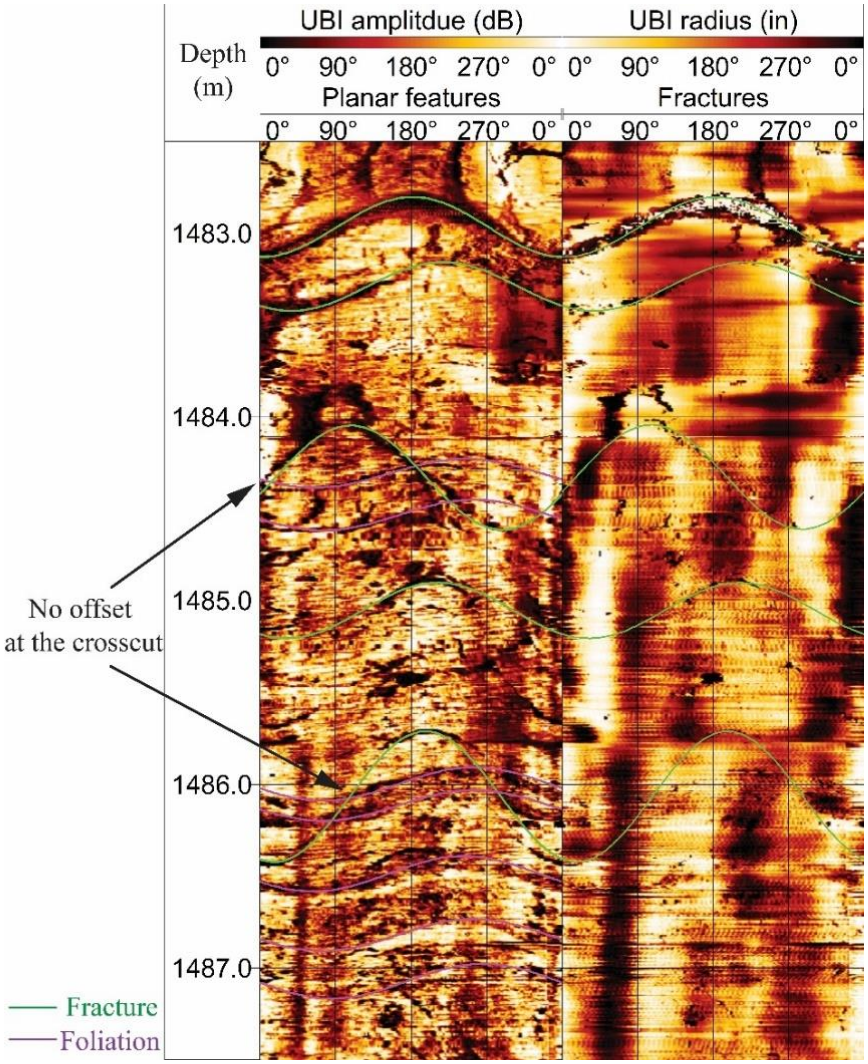

Figure S5. Planar features from UBI amplitude (left panel) and transit time (right panel) images. Green and purple sinusoids represent identified fractures and foliations respectively.

Table S3. Fractures Picked from UBI Image Logs

Depth (m)	Dip azimuth (°)	Dip angle (°)
1153.43	355.68	64.47
1159.22	124.30	75.21
1160.78	112.43	70.24
1481.18	84.75	46.13
1481.53	319.78	66.20
1482.96	3.20	53.05
1483.29	39.71	49.82
1484.33	288.15	66.71
1485.05	33.63	54.05
1486.07	17.85	72.18
1488.83	39.06	78.93
1537.39	351.34	55.79
1543.43	295.28	58.69
1543.58	291.51	57.70
1712.18	90.10	47.08
1712.27	88.42	51.00
1747.10	75.69	48.21
2183.42	58.11	68.51
2289.23	66.57	68.76
2311.59	9.12	65.15

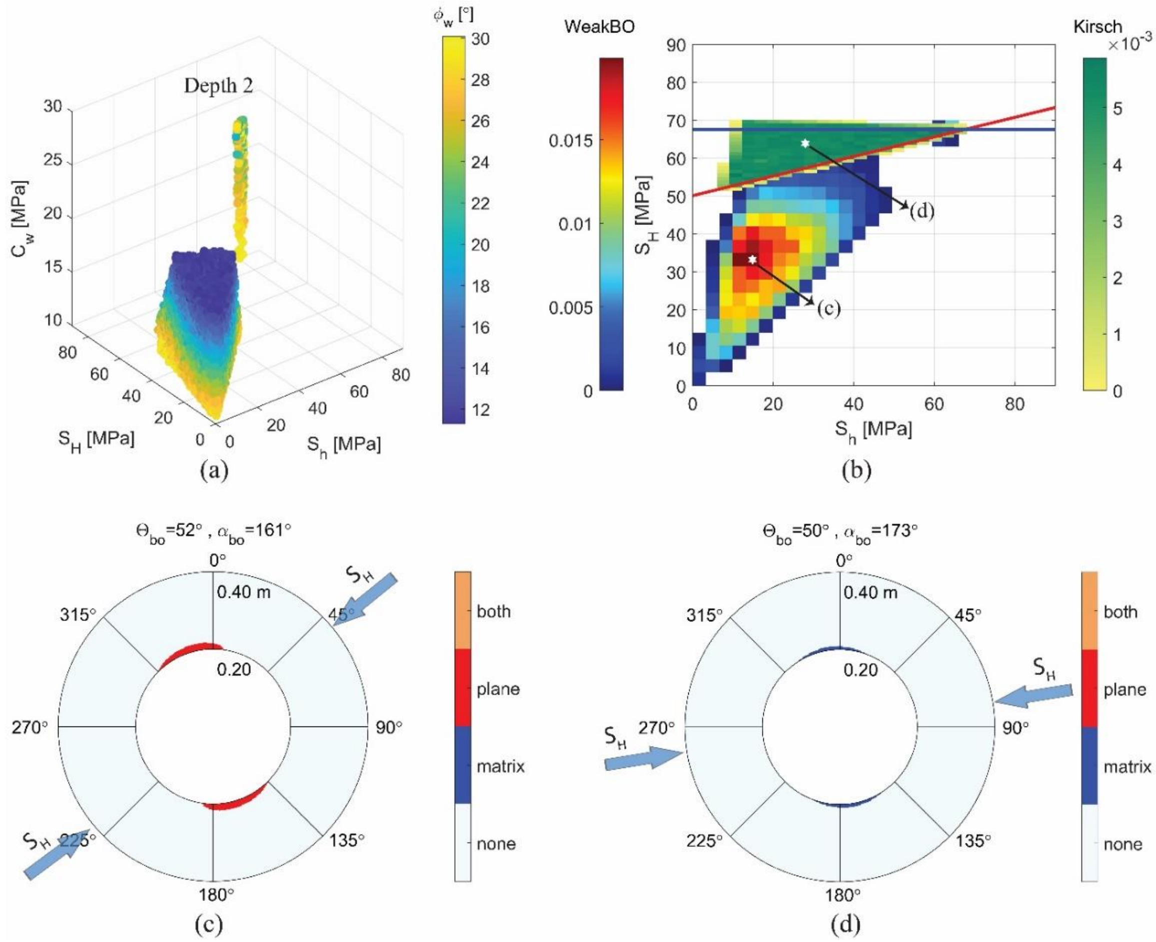

Figure S6. Feasible stress magnitudes and modelled failure patterns at the depth zone 2 (2000 m).

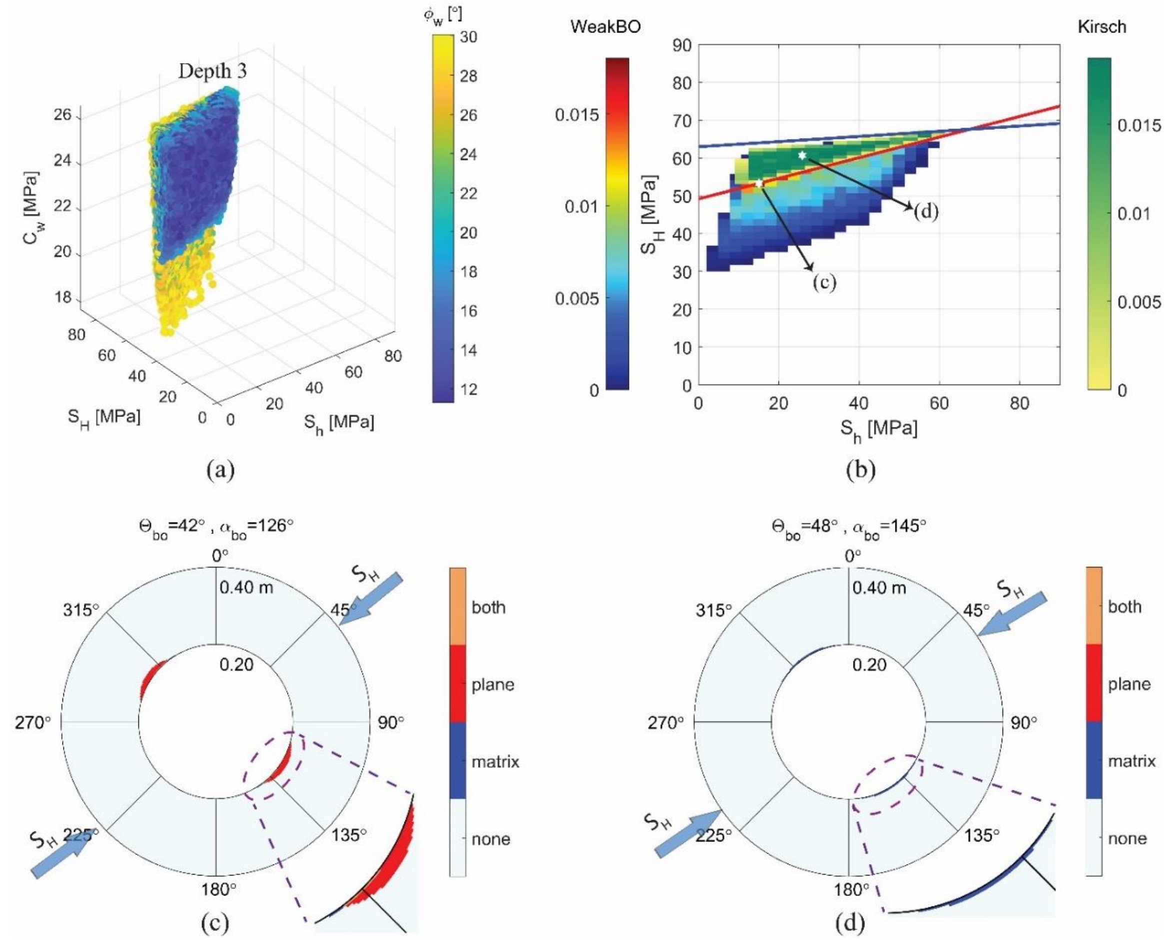

Figure S7. Feasible stress magnitudes and modelled failure patterns at the depth zone 3 (2210 m).

Text S4. Insensitivity of Equation 2

To reiterate, Eq. 2 is widely used to give estimates of the greatest horizontal compressive stress S_H if the unconfined compressive strength (UCS), the magnitude of the least horizontal compressive stress (S_h), and the full breakout width given as a circumferential angle Θ are known as per:

$$S_H = \frac{UCS - S_h(1 - 2\cos\Theta)}{1 + 2\cos\Theta}$$

Estimation of S_H remains difficult, and therefore the usage of this equation is popular as often S_h, UCS, and Θ can be measured through a combination of borehole and core measurements (Schmitt et al., 2012; Zoback et al., 2003).

In Figure S8, S_H is calculated as a function of Θ for S_h = 20 MPa and UCS = 135 MPa which are representative values found in the study. This plot shows that S_H is largely insensitive to the breakout width at least up to Θ ~45°, and this helps to explain the wide ranges of possible realizations in the modelling for the isotropic case.

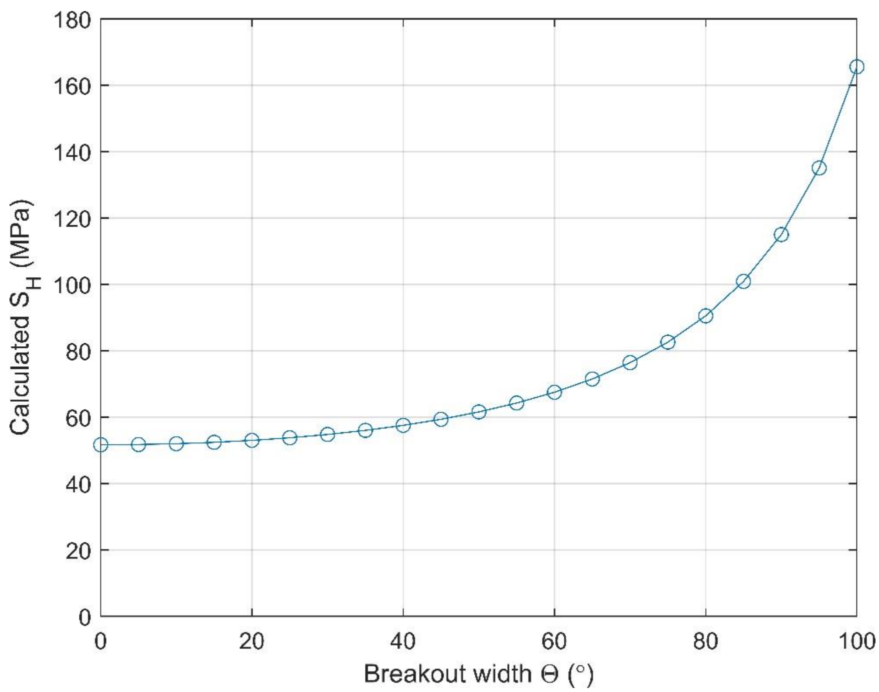

Figure S8. Calculated greatest horizontal compressive stress S_H as a function of breakout width Θ for the case with S_h = 20 MPa and UCS = 135 MPa according to Eq. 2.

Reference

Amadei, B. (1983). *Rock anisotropy and the theory of stress measurements*. Berlin: Springer-Verlag. https://doi.org/10.1007/978-3-642-82040-3

Azzola, J., Valley, B., Schmittbuhl, J., & Genter, A. (2019). Stress characterization and temporal evolution of borehole failure at the Rittershoffen geothermal project. *Solid Earth*, *10*(4), 1155–1180. https://doi.org/10.5194/se-10-1155-2019

Bell, J. S., & Gough, D. I. (1979). Northeast-southwest compressive stress in Alberta evidence from oil wells. *Earth and Planetary Science Letters*, *45*(2), 475–482. https://doi.org/10.1016/0012-821X(79)90146-8

Boness, N. L., & Zoback, M. D. (2004). Stress-induced seismic velocity anisotropy and physical properties in the SAFOD Pilot Hole in Parkfield, CA. *Geophysical Research Letters*, *31*(15), L15S17. https://doi.org/10.1029/2003GL019020

Boness, N. L., & Zoback, M. D. (2006). A multiscale study of the mechanisms controlling shear velocity anisotropy in the San Andreas Fault Observatory at depth. *Geophysics*, *71*(5), F131–F146. https://doi.org/10.1190/1.2231107

Brudy, M., & Zoback, M. D. (1999). Drilling-induced tensile wall-fractures: Implications for determination of in-situ stress orientation and magnitude. *International Journal of Rock Mechanics and Mining Sciences*, *36*(2), 191–215. https://doi.org/10.1016/S0148-9062(98)00182-X

Chan, J. (2013). *Subsurface geophysical characterization of the crystalline Canadian Shield in Northeastern Alberta: implications for geothermal development*. *Master thesis*. Edmonton: University of Alberta. https://doi.org/10.7939/R3BR8MQ6B

Chan, J., & Schmitt, D. R. (2015). Initial seismic observations from a deep borehole drilled into the Canadian Shield in northeast Alberta. *International Journal of Earth Sciences*, *104*(6), 1549–1562. https://doi.org/10.1007/s00531-014-1110-x

Fang, X., Cheng, A., & Fehler, M. C. (2015). Investigation of borehole cross-dipole flexural dispersion crossover through numerical modeling. *Geophysics*, *80*(1), D75–D88. https://doi.org/10.1190/geo2014-0196.1

Goswami, D., Roy, S., & Akkiraju, V. V. (2019). Delineation of damage zones from 3 km downhole geophysical logs in the Koyna Seismogenic Zone , Western India. *Journal of Geophysical Research: Solid Earth*, *124*(6), 6101–6120. https://doi.org/10.1029/2018JB017257

Goswami, D., Hazarika, P., & Roy, S. (2020). In situ stress orientation from 3 km borehole image logs in the Koyna Seismogenic Zone, western India: implications for transitional faulting environment. *Tectonics*, *39*(1), e2019TC005647. https://doi.org/10.1029/2019TC005647

Gough, D. I., & Bell, J. S. (1982). Stress orientations from borehole wall fractures with examples from Colorado, east Texas, and northern Canada. *Canadian Journal of Earth Sciences*, *19*(7), 1358–1370. https://doi.org/10.1139/e82-118

Hiramatsu, Y., & Oka, Y. (1962). Analysis of stress around a circular shaft or drift excavated in ground in a three dimensional stress state. *Journal of Mining and Metallurgy Institute of Japan*, *78*, 93–98.

Iturrino, G. J., Goldberg, D., Glassman, H., Patterson, D., Sun, Y. F., Guerin, G., & Haggas, S. (2005). Shear-wave anisotropy from dipole shear logs in oceanic crustal environments. *Geological Society Special Publication*, *240*, 117–131. https://doi.org/10.1144/GSL.SP.2005.240.01.10

Kerkela, S., & Stock, J. M. (1996). Compression directions north of the San Fernando Valley determined from borehole breakouts. *Geophysical Research Letters*, *23*(23), 3365–3368. https://doi.org/10.1029/96GL03054

Kirsch, E. G. (1898). Die theorie der elastizitat und die bedurfnisse der festigkeitslehre. *Zeitschrift Des Vereines Deutscher Ingenieure*, *42*(29), 797–807.

Majorowicz, J., Chan, J., Crowell, J., Gosnold, W., Heaman, L. M., Kück, J., et al. (2014). The first deep heat flow determination in crystalline basement rocks beneath the Western Canadian Sedimentary Basin. *Geophysical Journal International*, *197*(2), 731–747. https://doi.org/10.1093/gji/ggu065

Morin, M. L. (2017). *Natural and drilling induced fractures in the Grosmont Formation, Alberta: implications for the state of stress*. *Master thesis*. Edmonton: University of Alberta. https://doi.org/10.7939/R3B56DJ60

Schmitt, D. R., Currie, C. A., & Zhang, L. (2012). Crustal stress determination from boreholes and rock cores: fundamental principles. *Tectonophysics*, *580*, 1–26. https://doi.org/10.1016/j.tecto.2012.08.029

Sinha, B. K., Norris, A. N., & Chang, S.-K. (1994). Borehole flexural modes in anisotropic formations. *Geophysics*, *59*(7), 1037–1052. https://doi.org/10.1190/1.1443660

Stork, A. L., Nixon, C. G., Hawkes, C. D., Birnie, C., White, D. J., Schmitt, D. R., & Roberts, B. (2018). Is CO2 injection at Aquistore aseismic? A combined seismological and geomechanical study of early injection operations. *International Journal of Greenhouse Gas Control*, *75*, 107–124. https://doi.org/10.1016/j.ijggc.2018.05.016

Thomsen, L. (1986). Weak elastic anisotropy. *Geophysics*, *51*(10), 1954–1966. https://doi.org/https://doi.org/10.1190/1.1442051

Winkler, K. W. (1997). Acoustic evidence of mechanical damage surrounding stressed boreholes. *Geophysics*, *62*(1), 16–22. https://doi.org/10.1190/1.1444116

Wu, H.-Y., Ma, K.-F., Zoback, M. D., Boness, N., Ito, H., Hung, J.-H., & Hickman, S. (2007). Stress orientations of Taiwan Chelungpu-Fault Drilling Project (TCDP) hole-A as observed from geophysical logs. *Geophysical Research Letters*, *34*(1), L01303. https://doi.org/10.1029/2006GL028050

Wu, Y.-H., Yeh, E.-C., Dong, J.-J., Kuo, L.-W., Hsu, J.-Y., & Hung, J.-H. (2008). Core-log integration studies in hole-A of Taiwan Chelungpu-fault Drilling Project. *Geophysical Journal International*, *174*(3), 949–965. https://doi.org/10.1111/j.1365-246X.2008.03841.x

Zoback, M. D., Barton, C. A., Brudy, M., Castillo, D. A., Finkbeiner, T., Grollimund, B. R., et al. (2003). Determination of stress orientation and magnitude in deep wells. *International Journal of Rock Mechanics and Mining Sciences*, *40*(7–8), 1049–1076. https://doi.org/10.1016/j.ijrmms.2003.07.001